ELSEVIER

Contents lists available at ScienceDirect

Tribology International

journal homepage: www.elsevier.com/locate/triboint





Tailoring the tribo-corrosion response of (CrNbTiAlV)CxNy coatings by controlling carbon content

Dewen Niu ^{a,d}, Xiao Zhang ^{b,c,d}, Xudong Sui ^{b,c,d}, Zhiqiang Shi ^{a,*}, Xiaolong Lu ^{b,c,d}, Cong Wang ^{b,c,d}, Yanfang Wang ^a, Junying Hao ^{b,c,d,**}

- ^a School of Materials Science and Engineering, China University of Petroleum (East China), Qingdao 266580, China
- b Center of Materials Science and Optoelectronics Engineering, University of Chinese Academy of Sciences, Beijing 100049, China
- ^c Qingdao Center of Resource Chemistry and New Materials, Qingdao 266000, China
- d State Key Laboratory of Solid Lubrication, Lanzhou Institute of Chemical Physics, Chinese Academy of Science, Lanzhou 730000, China

ARTICLE INFO

Keywords: Magnetron sputtering Carbonitride Microstructure Tribo-corrosion

ABSTRACT

High-entropy carbonitrides exhibit excellent properties in friction and corrosion. Here, the tribo-corrosion response of (CrNbTiAlV)C_xN_y coating were studied in 3.5 wt.% NaCl solution at room temperature. The doping of carbon makes the coating structure dense. When the carbon content of the coating is 40%, the coating exhibits maximum hardness (20.21 GPa). As the carbon content increases, the synergistic effect of tribo-corrosion on the coating gradually weakens, and friction coefficient decreases. The coating with 40% carbon content has the smallest change in static and dynamic current density (0.14 $\times 10^{-8}$ A/cm²), the smallest friction coefficient (0.28), and the smallest wear volume loss. These results show that the coating can effectively protect the substrate in case of tribo-corrosion.

1. Introduction

Generally, in marine environment, oxygen and chlorine salts can cause corrosion of the mechanical metal parts posing a threat to the safe operation of the equipment. Therefore, choosing the right anti-corrosion material is essential to prolong the service life of the machine [1]. So far, many corrosion-resistant alloys have been developed, such as stainless steel [2–4], Ni alloys [5,6], Ti alloys [7,8], and Al alloys [9–11]. Among them, 316 L has a dense passivation film formed on the surface due to its high Cr content, showing excellent corrosion resistance. So 316 L stainless steel is widely used in marine moving parts. However, the working condition of marine moving parts is to operate under load in seawater, which is affected by both friction and corrosion at the same time. The applied load will destroy the passivation film formed on the surface of the alloy and accelerate the corrosion damage of the alloy. Based on our previous research, 316 L did not perform well under friction and corrosion [12]. In order to improve the tribo-corrosion performance of 316 L, one of the most effective solutions is to apply a protective coating on the surface of 316 L.

One of the coating materials is the high-entropy alloys (HEAs)

proposed by Ye et al. [13]. HEAs are uniformly distributed replacement solid solution alloys formed by five or more elements, and the percentage of each element is between 5% and 35%. In recent years, there have been more and more studies on various aspects of high-entropy alloys [14-17]. Compared with traditional alloys, high-entropy alloys exhibit high hardness [18,19], good wear resistance [20,21], good corrosion properties [22-24], and good thermal stability [25,26]. However, the development and application of HEAs bulk is limited due to the limitation of size and the complexity of fabrication process [27]. The substrate is coated with a high-entropy alloy coating (HEAC) as one solution to the problem. Thus, High-entropy alloy coatings are further developed [28,29]. Compared with the bulks, the HEACs exhibit superior mechanical properties and corrosion resistance due to reduced material dimensionality. Fang et al. [30]. found that the CoCrFeMnNiV_x coating has ultra-fine grains and a large number of twins, showing higher hardness compared to the bulk. Recently, Zheng et al. [31]. prepared a VAlTiCrSi coating on the surface of 304 by DC magnetron sputtering. The coating exhibits an amorphous structure with a smooth and dense surface. Compared with 304, the coating has a lower current density $(4.68 \times 10^{-9} \text{ A/cm}^2)$ and exhibits excellent corrosion resistance.

^{*} Corresponding author.

^{**} Corresponding author at: Center of Materials Science and Optoelectronics Engineering, University of Chinese Academy of Sciences, Beijing 100049, China. E-mail addresses: szqiang@upc.edu.cn (Z. Shi), jyhao@licp.cas.cn (J. Hao).

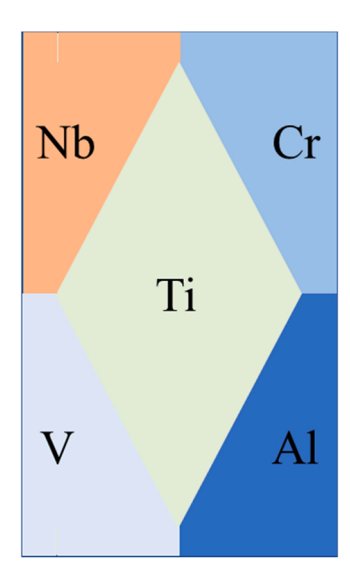


Fig. 1. The schematic diagram of splicing target.

It was found that the doping of Ag reduced the corrosion rate of $Ti_{1.5}ZrTa_{0.5}Nb_{0.5}W_{0.5}$ HEAC by 2.3–2.8 orders of magnitude and greatly enhanced the polarization resistance of the coatings by Alamdari et al. [32]. Khan et al. [33]. found that AlCoCrCu_{0.5}FeNi prepared at a working pressure of 10 mTorr had a mixed structure of FCC and BCC. The protective oxide film Al_2O_3 and Cr_2O_3 formed on the surface makes the coating have high resistivity.

Recently, carbon and nitrogen doping of HEACs has become a hot topic. Due to the relatively small size of nitrogen atom, the coatings will have solid solution strengthening and the mechanical properties will be improved [34-37]. Xia et al. [35] prepared a series of (MoN $bTaVW)_xN_{1-x}$ coatings with different nitrogen contents by cathodic arc deposition and DC magnetron sputtering, respectively. It was found that with the increase of nitrogen flow, the crystal structure of the coating changed from BCC to FCC, and the maximum hardness reached 30 GPa. Li et al. [38] found that the (NbTaMoW)N_x coating exhibited a minimum wear rate of $5 \times 10^{-7} \text{ mm}^3/\text{N} \cdot \text{m}$ when x = 0.48. Carbon doping can enhance the friction performance of the coating and reduce the coefficient of friction. The carbon doping also enhances the corrosion resistance of the coating. Kao et al. [39] prepared carbon-doped CrNbSiTaZr coatings by passing acetylene gas. When the acetylene flow rate is 19 sccm, the friction coefficient of the coating is 0.05, and the wear rate reaches $0.16 \times 10^{-6} \text{ mm}^3/\text{N·m}$. Medina et al. [40] fabricated (CoCrFeMnNi)_xC_{1-x} coatings by a non-equilibrium magnetron sputtering system. They found that the carbon close to the coating surface enhanced the coating's corrosion resistance. Most recent articles have focused on the single effect of friction or corrosion on materials. But there are many marine moving parts that work under a combination of corrosion and applied loads. The synergistic effect of friction and corrosion on materials can also have an impact on material failure.

Few articles have investigated the response of materials under the combined influence of friction and corrosion. Therefore, according to the previous study [23,24,41], the magnetron sputtering method was adopted to prepare the (CrNbTiAlV)C $_x$ N $_y$ coating in this paper, using a five-element splicing target and a piece of graphite target. The carbon content of the (CrNbTiAlV)C $_x$ N $_y$ coatings was controlled by adjusting the current of the graphite target. The microstructure, tribological properties and tribo-corrosion performance of the coatings were investigated studied.

 $\label{eq:continuous_continuous_continuous} \textbf{Table 1} \\ \textbf{Deposition parameters of (CrNbTiAlV)} C_x N_y \ coating \ by \ magnetron \ sputtering \ system.}$

Deposition parameters	Values
Splicing target current (A)	4.5
C target current (A)	1, 2, 3 and 4 for S1, S2, S3, S4 respectively
Working pressure (Torr)	3.8×10^{-3}
Bias voltage (V)	-126
Ar flow (sccm)	18
N ₂ flow (sccm)	38
Deposition time (min)	210, 180, 150 and 120

2. Experimental details

2.1. $(CrNbTiAlV)C_xN_y$ coatings preparation

(CrNbTiAlV)CxNv coatings were sputtered on the prepared 316 L substrate and on Si wafers using an unbalanced magnetron sputtering system (UPD-650, Teer). In the substrate preparation process, the 316 L substrate was polished to a bright surface without obvious defects. The roughness of the substrate is less than 10 nm. Si wafer were laser-cut into rectangles of equal-size rectangles for cleaning and clamping. The 316 L and Si wafers were washed four times alternately with alcohol and petroleum ether. Each wash took 15 min to insure the surfaces clean. Two C targets (99.9 at.%), one Cr target (99.9 at.%) and one five metal (Ti, Al, Cr, Nb, V) splicing target (99.9 at.%) were selected to deposit the coatings. The figure of splicing target is shown in Fig. 1. The substrates were fixed in the middle of the rack to ensure the same coating was produced. The rotating speed of the rack was 5 rpm during the experiment. Before the process starts, the air pressure in the chamber is pumped to less than 3×10^{-5} Torr. The process is divided into three steps. First, the surfaces of the substrate and the target were cleaned with Ar^+ for 30 min. The set voltage of the targets was - 450 V. In the second step, the time for depositing a Cr transition layer on the surface of the substrate by using the Cr target was 8 min. In the last step, nitrogen gas was introduced while the currents of the C target and the spliced target were increased to the set values, respectively. Table 1 shows the process parameters of the deposited coating. In order to ensure the same thickness of coatings, the process time of the last step is different. To better distinguish each coating, the (CrNbTiAlV)CxNv coatings are named S1, S2, S3 and S4, from small to large according to the C content in the coatings.

2.2. Characterization of $(CrNbTiAlV)C_xN_y$ coating

Coatings deposited on Si wafers were observed by scanning electron microscopy (FESEM, JSM, 7610 F) for cross-sectional microstructure and thickness of the coatings. Energy Dispersive Spectroscopy (EDS, Thermo Scientific) is used to observe the distribution of elements in the sample. Electron probe microscope analyzer (EPMA, JXA-8530 F PLUS)

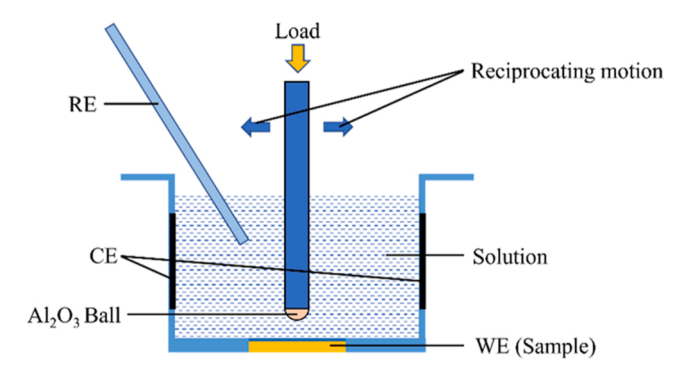


Fig. 2. Tribo-corrosion machine model.

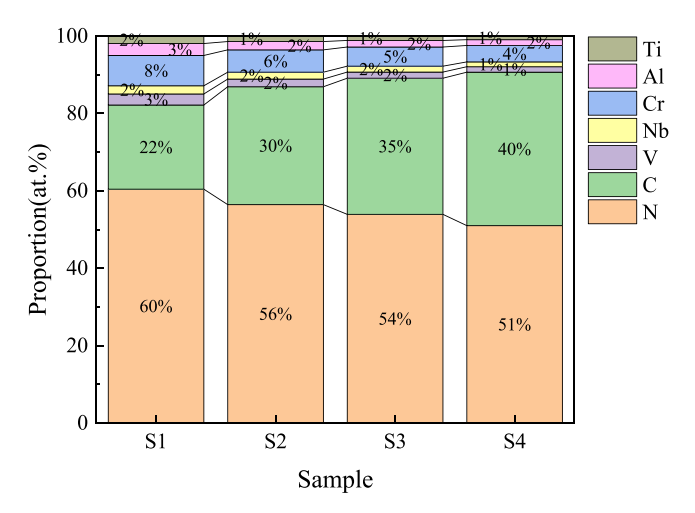


Fig. 3. Chemical compositions (at.%) of the samples.

was used to analyze the elements and content of the coating. The crystal structure of the coatings was determined by X-ray diffraction (XRD, Bruker D 8 Advance). And the scanning angle of XRD was from 20° to 60° . The hardness (H) and elastic modulus (E) of the coatings were characterized with a nano indenter (UNHT3, Anton Paar). The test mode used the fixed loading force mode, and the loading force was set to 20 mN. Six points were tested for each coating to ensure to get correct data. The carbon bonds of the coatings were measured by Raman spectrum (DXR2, Thermo) with 532 nm laser.

2.3. Corrosion performance testing of (CrNbTiAlV) C_xN_y coating

The electrochemical properties and tribo-corrosion properties performance of the samples were tested by a linear reciprocating friction machine with a three-electrode system (MFT-4000, Lanzhou Huahui). The structure of the instrument is shown in Fig. 2. The prepared coating was the working electrode (WE), Ag/AgCl was used as the reference electrode (RE), and carbon was the counter electrode (CE). Al₂O₃ ball (Φ 6 mm) was chosen as the friction pair. The experiments were characterized in 3.5 wt.%NaCl solution at room temperature. The exposed area of the coating was 2.25 cm². When testing the electrochemical properties of all coatings, the samples were soaked for at least 1 h to stabilize the surface state of the coatings. Tribo-corrosion tests were conducted to test coatings at open circuit potential (OCP). In order to reach a steady state, the coating was first soaked for 10 min. Then slid for 40 min under load and soaked for 10 min after removing the load. The load in tribocorrosion was 1 N and the sliding frequency was 0.1 Hz. The stroke value was 6 mm. In static polarization test and potentiodynamic polarization (PDP) test, the sweep range was from -0.6 V to +0.6 V relative to the reference electrode. The scanning speed was 0.5 mV/s to ensure that experiment time was 40 min. SEM and EDS were used to characterize the morphology and elemental composition of the wear track after the tribo-corrosion test. The volume loss cause by friction were tested with a 3D profilometer (MicroXAM 800, America).

3. Result and discussion

3.1. Structure and mechanical characterization of (CrNbTiAlV) C_xN_y coating

Fig. 3 shows the results of the elemental composition of the (CrNbTiAlV) C_xN_y coatings. Obviously, the carbon content in the coating gradually increases from 22 at.% to 40 at.% with increasing carbon target current. This is because as the current increases, the carbon atoms gain more kinetic energy and thus the carbon deposition rate gradually increases. The N element content fluctuates between 51 at.% and 60 at.

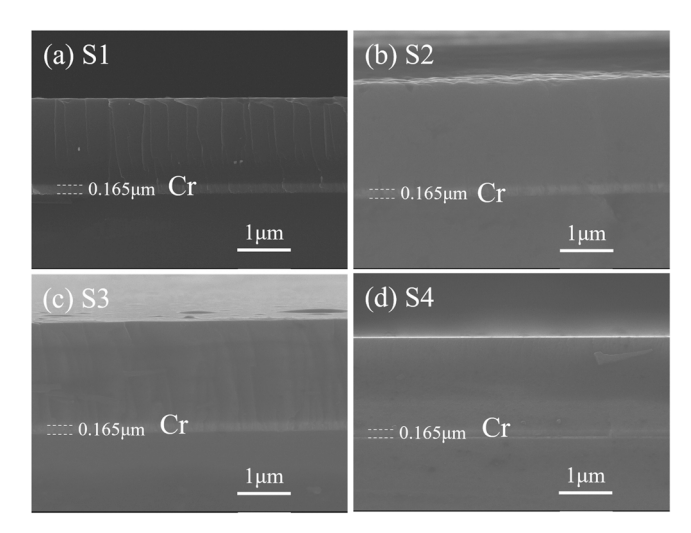


Fig. 4. Cross-sectional SEM images of $(CrNbTiAlV)C_xN_y$ coating (a) S1; (b) S2; (c) S3; (b) S4.

%, which basically accounts for half of the entire element of the coating. With the increase of carbon target current, the proportion of other elements in the coating gradually decreased.

The SEM cross-sectional morphology of the coating is shown in Fig. 4. As can be seen from the figure, all the coatings exhibit a dense microstructure, which means that the change of carbon content has no obvious effect on the structure of the coating. The columnar structure typical of PVD is not exhibited. By adjusting the process time, the thickness of the Cr transition layer is all 0.165 μm , and the thickness of the coating is basically about 2 μm . S2 was selected to test EDS mapping to observe the element distribution in the sample. The test results are shown in Fig. 5. It can be seen that the elements in the sample are evenly distributed. Cr is concentrated at the bottom of the sample, which is the Cr transition layer.

Fig. 6 presents the XRD results of the prepared samples. The crystallographic orientations of all coatings are (111) and (200) corresponding to the angles of 33.08° and 44.16° , and the coatings contain carbonitrides. The crystallographic orientation the coating don not change significantly with increasing carbon content. This indicates that the carbonitride content in the coating is unchanged.

Fig. 7(a) shows the hardness and elastic modulus test results of the (CrNbTiAlV)CxNv coating. It can be clearly seen that the hardness of the coating increases gradually with the increase of carbon content. The elastic modulus first decreased with the increase of carbon content and then maintained at a certain level. The maximum hardness and elastic modulus of the coating reached 20.21 GPa. And the elastic modulus of the coating reached 174.09 GPa. The carbon increases the degree of lattice distortion of the coating, and the hardness of the coating increases. Generally speaking, H/E indicates the strength of the material to resist fracture [42] and H³/E² indicates the strength of the material's ability to resist plastic deformation [43]. Fig. 6(b) shows the calculated H/E and H³/E² values for (CrNbTiAlV)C_xN_y coatings. It is obvious that the H/E and H³/E² values of the coatings increase with increasing carbon content. The H/E and H³/E² values of S4 were the largest, reaching 0.12 and 0.32. This indicates that the (CrNbTiAlV)CxNy coatings have strong fracture resistance and plastic deformation resistance. Among them, the S4 coating has the most excellent mechanical properties.

Raman spectra is commonly used to test the microstructure of carbon-containing coatings. Fig. 8(a) shows the Raman spectra of (CrNbTiAlV)C_xN_y coatings. Two Gaussian peaks make up the Raman spectrum: the D peak and the G peak are at 1380 and 1568 cm⁻¹ respectively [44]. Fitting the Raman spectral results of the coating by Gaussian fitting are shown in Fig. 8(b). It can be seen that the intensity ratio of D peak to G peak (I_D/I_G) gradually decreases with the increase of

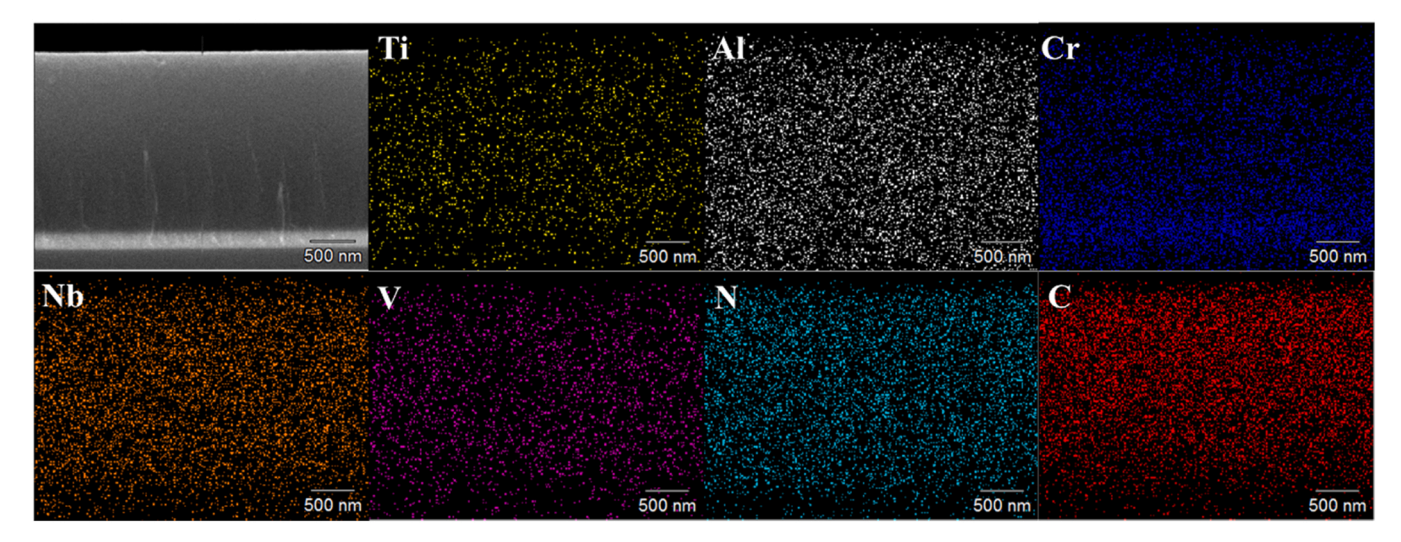


Fig. 5. EDS mapping of (CrNbTiAlV)C_xN_v coating.

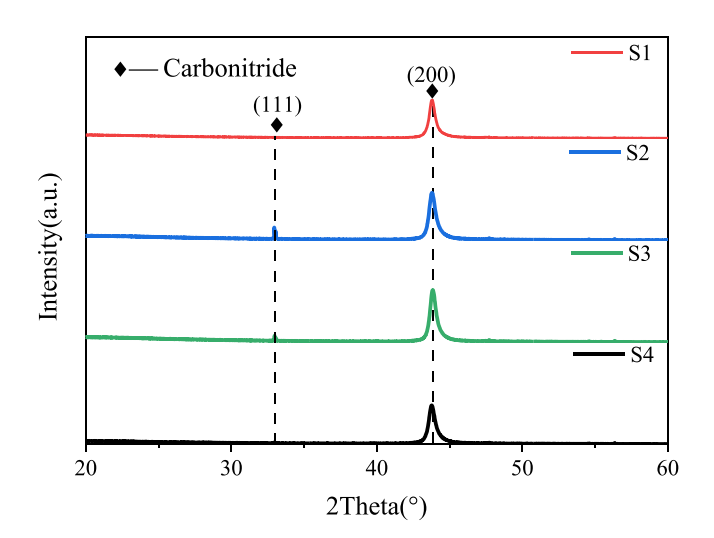
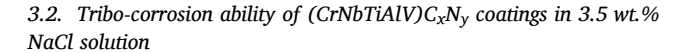


Fig. 6. XRD patterns of (CrNbTiAlV) C_xN_y coating.

carbon current. The I_D/I_G value of the coating gradually decrease from 3.07 to 1.24. The position of the G peak is the smallest when the carbon content is the largest, which is $1521.60~\text{cm}^{-1}$. The more sp^3 clusters in the coating, the higher the hardness of the coating [45]. The ratio of I_D/I_G corresponds to the ratio of sp^2/sp^3 [46,47]. Therefore, the hardness of the coating increases with increasing carbon content.



3.2.1. Effect of sliding wear under OCP

In the case of OCP, the friction coefficient and potential change of the (CrNbTiAlV)CxNv coatings tribo-corrosion performance are shown in Fig. 9. It is clearly that the coating is already in a stable state at the OCP before tribo-corrosion. When the load is applied, the potential of the sample decreases to different degrees, and gradually becomes stable with the friction. When the load is removed, the potential of the samples all increase to different degrees. This is because the passivation film is formed on the samples surface before loading and reaches a stable state, and the passivation film is destroyed after loading. Destruction of the passivation film leads to a drop in potential [48,49]. During tribo-corrosion, the generation rate of the passivation film on the sample surface and the removal rate forms a dynamic equilibrium, so the potential of the sample is gradually stabilized [50]. When the load is removed, a new passivation film is formed on the surface of the sample, which increases the potential of the sample [51]. Among them, the potential change of 316 L is the largest, and the change range is - 0.21 V. With the increase of carbon content, the potential change degree of the sample becomes smaller. The potential changes of S1 and S2 are similar. The potential change of the S4 coating is minimal and almost unchanged. This is because the carbon doping enhances the inertness of (CrNbTiAlV)CxNv coatings and thus reduces the sensitivity of the coating potential to friction.

Fig. 9(b) presents the friction coefficient of 316 L substrate and coating samples in tribo-corrosion test under OCP condition. When the carbon content of the coating increases from 22 at.% to 40 at.%, the

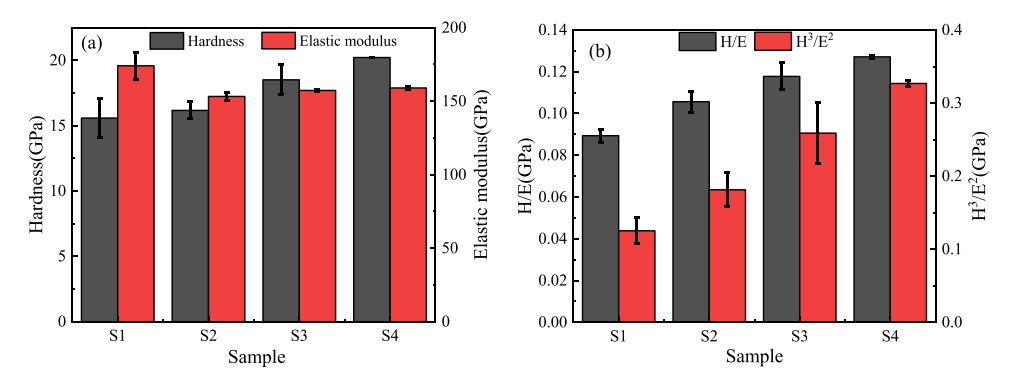


Fig. 7. (a) Hardness and elastic modulus and (b) H/E and H^3 / E^2 .

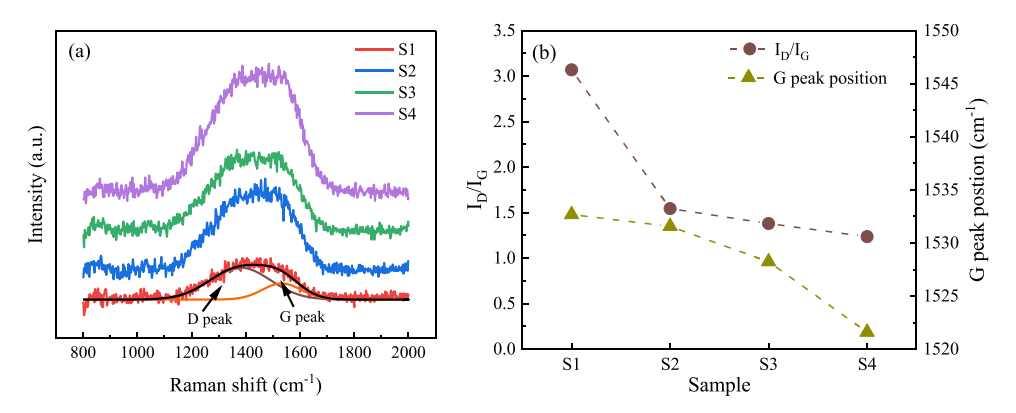


Fig. 8. (a) Raman spectra and (b) I_D/I_G , fitted G peak position of (CrNbTiAlV) C_xN_y coatings.

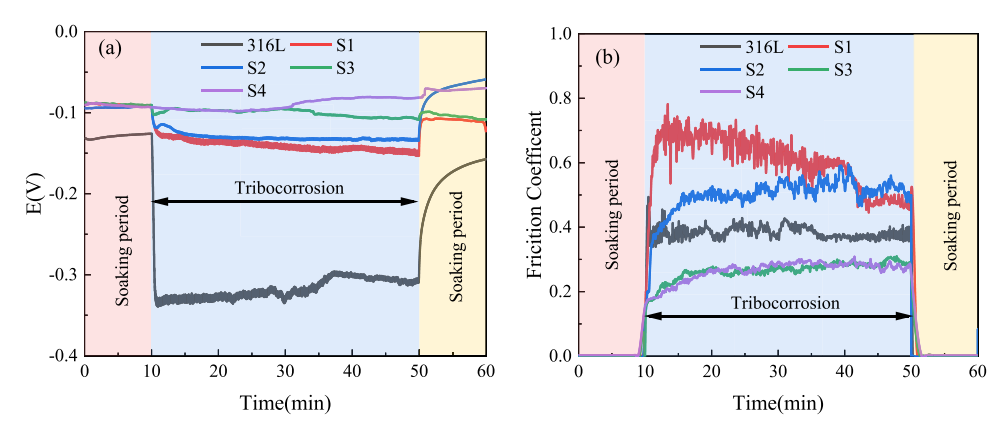


Fig. 9. (a) potential change under OCP and (b) friction coefficient curves of (CrNbTiAlV) C_xN_y coatings sliding against Al_2O_3 balls in 3.5 wt.% NaCl solution.

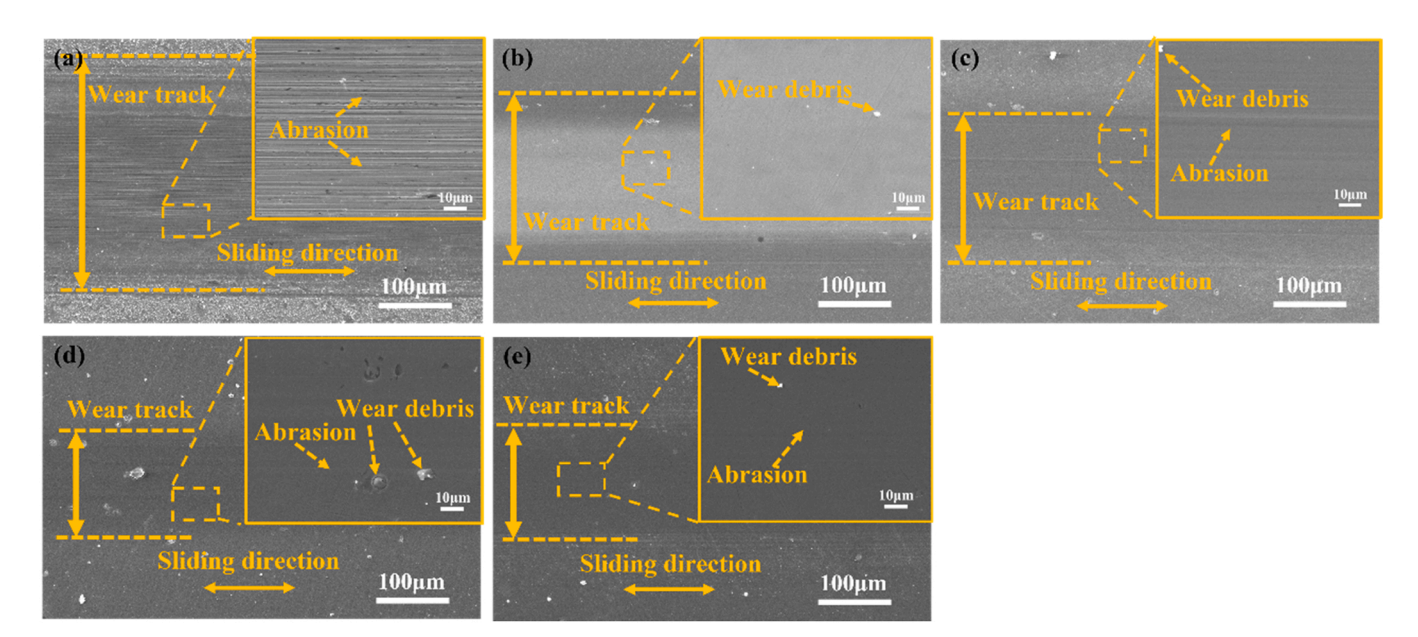


Fig. 10. SEM images of wear tracks for 316 L alloy and (CrNbTiAlV)C_xN_y coatings under OCP condition. (a) 316 L; (b) S1; (c) S2; (d) S3; and (e) S4.

coefficient of the coating decreases from 0.5 to 0.28. It can be seen that the friction coefficient of 316 L in the stable stage is lower than S1 and S2, but higher than S3 and S4, which means that different carbon content has a significant effect on the friction coefficient of the coating. Due to the low carbon content of S1 and S2, the effect on reducing the friction coefficient is limited. Therefore, the friction coefficients of S1 and S2 are higher. For S3 and S4 coatings with higher carbon content, they not only

have higher hardness, but also have lower friction coefficient during the friction process due to the lubricating effect of free carbon element. Therefore, in the case of open circuit potential, S3 and S4 can effectively protect the $316\,L$ substrate.

To further explain the tribo-corrosion mechanism of the samples at OCP, Fig. 10 shows the images of the wear tracks of each sample. The $316 \, L$ has the widest wear scar and the most severe wear. It can be seen

Table 2Element type and content of wear tracks after the tribo-corrosion test under OCP.

coating	Chemical composition (at.%)							
	Ti	Al	Cr	Nb	V	С	N	О
S1	2.1	3	13.3	2.3	2.8	19.5	52.8	4.2
S2	2	3.2	11.3	3.4	3.2	30.4	46.3	0.3
S3	1.5	2.6	9.7	2.7	3	35.2	44.9	0.3
S4	1.5	2.5	7.7	2.2	2.9	39.6	43.6	0

from Fig. 10(a) that the wear track shape of 316 L is furrow-like, which is abrasion. With the increase of carbon content, the width of wear scar gradually narrowed. As the hardness of the coating increases, the wear debris on the surface of the wear debris increases gradually. Carbon doping reduces the friction coefficient of the coating, and at the same time reduces the sensitivity of the coating to potential changes in the process of frictional corrosion [52]. So, the coatings have good tribo-corrosion performance.

Table 2 shows the wear track composition of the coatings after tribocorrosion under OCP. It is obvious that the oxygen content on the wear scar decreases with the increase of carbon content. This shows that the friction corrosion property of the coating is gradually enhanced. The wear track oxygen content of S4 is very low. According to the above results, S4 has the best friction performance under OCP.

3.2.2. Tribo-corrosion ability under PDP

Fig. 11(a) and (b) are the polarization curves of 316 L and the $(CrNbTiAlV)C_xN_y$ coatings under static polarization and PDP. It can be seen from Fig. 11(a) and (b) that 316 L is broken down under static polarization and dynamic polarization, and the breakdown potential is 0.2 V and 0.3 V, respectively. Simultaneously, there is no obvious breakdown phenomenon of the $(CrNbTiAlV)C_xN_y$ coatings in the polarization test, indicating that the corrosion resistance of the coatings

are better than that of the 316 L substrate.

The self-corrosion potential (E_{corr}) and self-corrosion current density (I_{corr})of each sample can be calculated by Tafel extrapolation, which are listed in Table 3. Generally speaking, The better the corrosion resistance of the material, the higher the E_{corr} and the lower the I_{corr} . [31]. Under static polarization conditions, the Ecorr of all prepared coatings are higher than that of the 316 L substrate and the Icorr of all coatings are lower than that of the 316 L substrate. Among them, the E_{corr} (-0.10 V) of S1 is the highest, and the I_{corr} (1.68 $\times 10^{-8}$ A/cm²) of S2 is the smallest. The I_{corr} of each sample increased to varying degrees compared to the static current density. Compared with the current density under static polarization, the current density of each sample under PDP has different degrees of increase. The level of current density can indicate the corrosion rate. Compared with the current density under static polarization, the current density of each sample under dynamic polarization has different degrees of increase. The increase in current density indicates that friction increases the corrosion rate of the material. Under the PDP condition, the I_{corr} of the 316 L substrate changes by two orders

Table 3 Dynamic polarization results of (CrNbTiAlV) C_xN_y coatings in 3.5 wt.% NaCl solution.

Condition	Sample	I _{corr} (A/cm ²)	E _{corr} (V)
Static Corrosion	316 L	3.55×10^{-8}	-0.20 V
	S1	2.69×10^{-8}	-0.10 V
	S2	1.68×10^{-8}	-0.14 V
	S3	2.28×10^{-8}	-0.12 V
	S4	3.24×10^{-8}	-0.13 V
Sliding Corrosion	316 L	1.72×10^{-6}	-0.27 V
-	S1	1.10×10^{-7}	-0.21 V
	S2	7.35×10^{-8}	-0.19 V
	S3	2.73×10^{-8}	-0.14 V
	S4	3.38×10^{-8}	-0.13 V

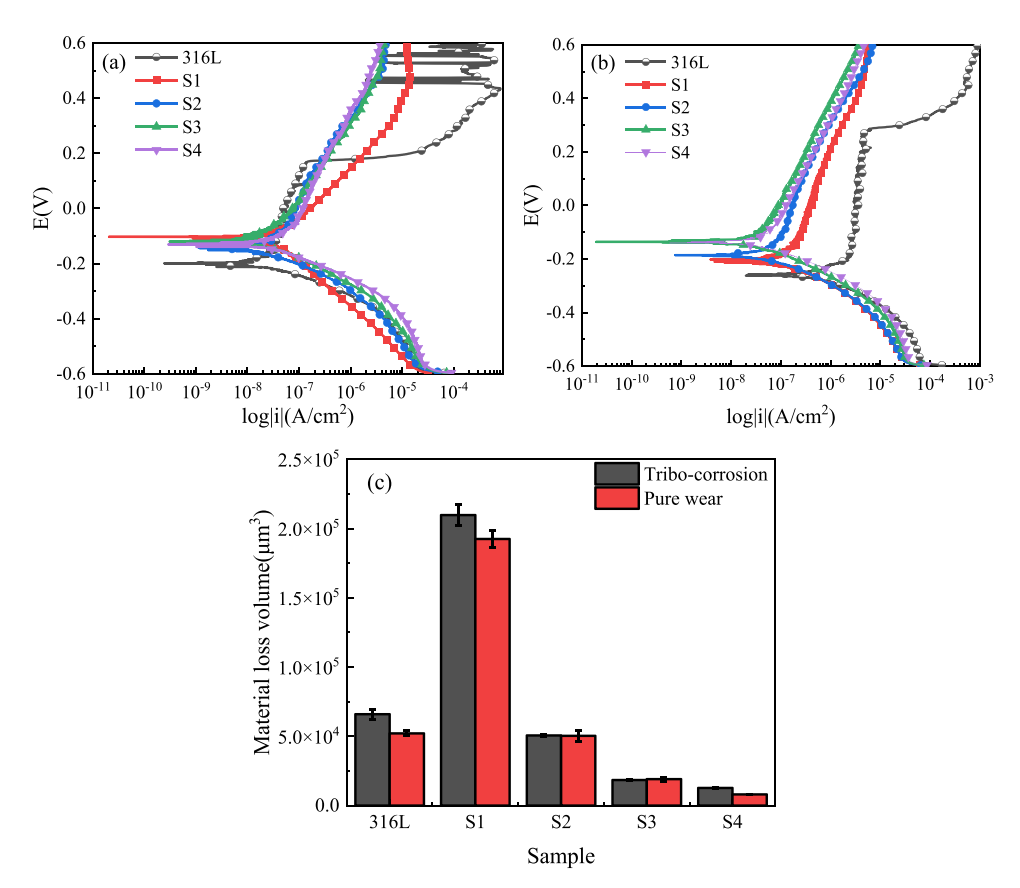


Fig. 11. Polarization curves under the condition of (a) pure corrosion and (b) tribo-corrosion; (c) wear volume of the samples under pure friction and PDP conditions.

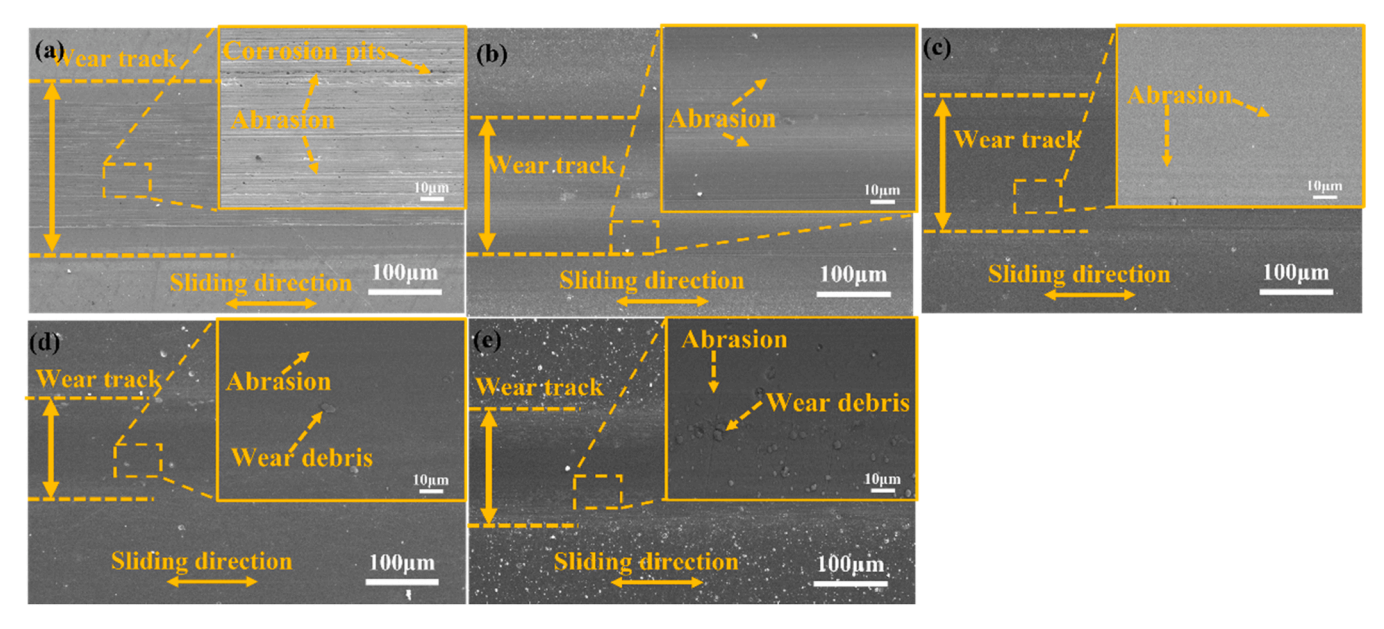


Fig. 12. SEM images of wear track of prepared coatings after tribo-corrosion tests in 3.5 wt.% NaCl solution. (a) 316 L; (b) S1; (c) S2; (d) S3; and (e) S4.

Table 4Element type and content of wear tracks after the tribo-corrosion test under PDP.

coating	Chemical composition (at.%)							
	Ti	Al	Cr	Nb	V	С	N	О
S1	2.1	2.6	5.6	3	3.9	28.2	49	5.6
S2	2.2	2.8	11.4	2.8	3.7	30.7	45.9	0.4
S3	1.5	2.7	11.9	2.8	2.3	33.1	44.9	0.7
S4	1.6	2	9.3	2.3	1.9	38.3	44.6	0

of magnitude, and the variation of the I_{corr} of the (CrNbTiAlV)CxNy coatings is smaller than that of the 316 L substrate. With the increase of carbon content, the potential variation of the sample decreases. The current density change of S4 is only $0.04\times 10^{-8} A/cm^2.$

Fig. 11(c) shows the material loss volume of substrate and coating samples under tribo-corrosion and pure wear condition, respectively. As shown in the picture, the wear volume loss of coating decreases with the increase of carbon content. Compared with other samples, S1 has the highest wear volume, which is due to the combined effect of its lower carbon content and lower hardness. Furthermore, the surface chemical stability of S1 is greatly affected by friction. Friction results in a large decrease in the corrosion current density of S1, which further intensifies the wear, leading to serious wear. Therefore, the wear volume of S1 is the largest compared with other samples.

The wear track morphologies of each sample after PDP are presented in Fig. 12. The most serious wear track on the 316 L substrate is abrasion, and pitting pits appear on surface. The type of wear for all coatings is abrasion. As the carbon content increases, the wear volume of the prepared coating decreases gradually. After the Al₂O₃ ball contacts the coating surface, the coating is subjected to normal stress and shear stress. The exfoliation of carbonitride plays a role of lubrication and reduces the wear volume of the coating. To further investigate the products of the coatings after tribo-corrosion under PDP, the element type and content of wear scars are detected by EDS. The test results are shown in Table 4. It can be seen that the oxygen content on the surface of the coating is very small. Due to the very low oxygen content, the wear scar surface of S2 and S3 shows 0 at.%. The oxygen content of the S4 wear scar surface is also only 0.9%. The graphite on the surface of the coating prevents oxidation of the metal in the coating and enhances the corrosion resistance of the coating. This also explains the good tribocorrosion properties of the coatings.

3.3. Tribo-corrosion mechanism of $(CrNbTiAlV)C_xN_y$ coatings

During the experiments, we assumed that corrosion only occurred on the wear track to better study the synergistic mechanism of friction and corrosion. [53,54]. Waston et al. [55] found that in the process of tribo-corrosion, the loss of material is not simply a superposition of the volume loss caused by corrosion and friction. Friction and corrosion interact with each other in the process of tribo-corrosion. Friction destroys the surface state of the material and accelerates the corrosion rate of the material. In the same way, the corrosion of the material will also change the state of the surface of the material, resulting in the change of the friction properties. Therefore, Waston et al. proposed that the volume lost during the tribo-corrosion process of the material is composed of the volume loss caused by pure wear, pure corrosion and the synergy of friction and corrosion. The volume loss caused by the tribo-corrosion process can be expressed by the following formula:

$$T = \Delta W + \Delta C \tag{1}$$

$$\Delta W = W + W_C \tag{2}$$

$$\Delta C = C_0 + C_W \tag{3}$$

$$T = W + W_C + C_0 + C_W$$
 (4)

Where T is the total volume of material lost during test. ΔW is the loss of material due to friction during test. ΔC is the volume loss due to corrosion. W is the volume loss of the material due to pure friction in the absence of corrosion. W_C is the volume of change between the volume of material lost by pure wear and the volume produced by friction in the process of test. C_W is the change between the volume loss caused by pure corrosion and the volume loss due to corrosion of the material during tribo-corrosion. The ΔW is measured by the three-dimensional topography instrument, and the results are shown in Fig. 11(c). The ΔC of the material can be calculated by the following formula:

$$C_0 = \frac{itM}{nF\rho} \tag{5}$$

Among them, i (A) is the corrosion current of the material in the tribo-corrosion experiment, which can be calculated from the data in Table 3. And t (s) is the experimental time from the applied potential, M (g/mol) is the average molar mass of the material, ρ (g/cm³) is the density of the material, ρ is the number of electrons lost by the sample during the experiment. F (C/mol) is Faraday's constant.

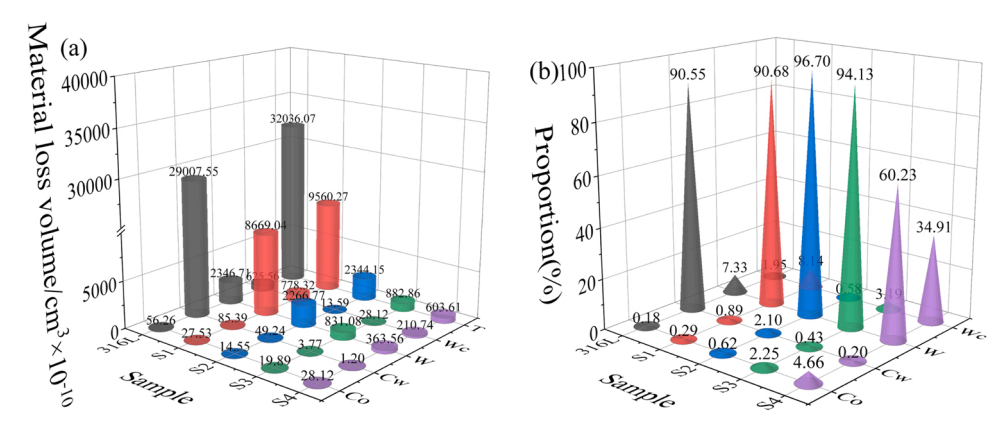


Fig. 13. (a) The volume and (b) proportion of each contribution of tribo-corrosion components for 316 L alloy and (CrNbTiAlV) C_xN_y coatings sliding against Al_2O_3 balls under polarization condition in 3.5 wt.% NaCl solution.

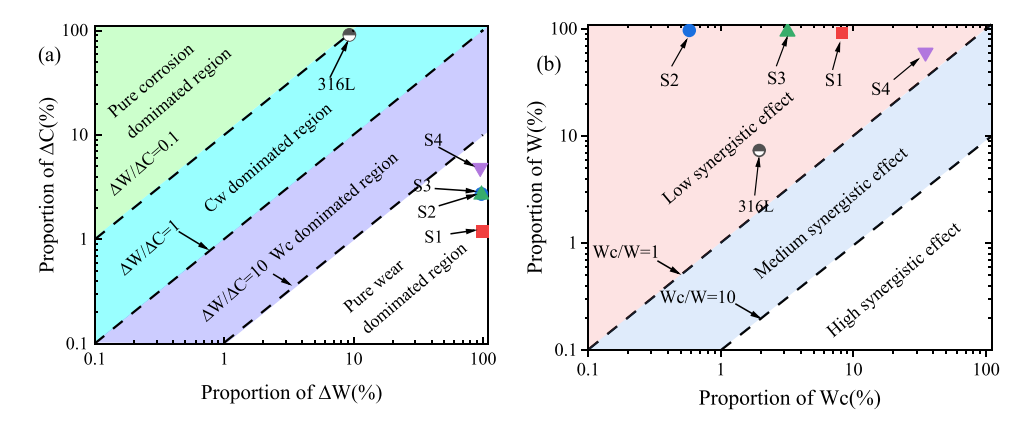


Fig. 14. (a) Wear-corrosion dominant graph and (b) degree of synergism with W_c proportion versus W proportion for tribo-corrosion of 316 L and S1, S2, S3 and S4 in 3.5 wt.% NaCl solution.

The calculation results of 316 L and (CrNbTiAlV)CxNv coatings are shown in Fig. 13. It can be seen that the T of 316 L after the tribocorrosion is much larger than that of the coating, which is two orders of magnitude larger than the loss of S4 with the minimum volume loss. The large volume loss of 316 L is due to the large increase in corrosion $(C_W, 90.55\%)$. This phenomenon shows that in the process of tribocorrosion of 316 L, the damage to the surface of 316 L caused by friction is serious, resulting in a huge change in the ΔC . The tribo-corrosion performance of 316 L is poor relative to the (CrNbTiAlV)C_xN_y coatings. With the increase of carbon content, the T of the coating during tribocorrosion decreases. S4 has the smallest total loss volume $(6.0361 \times 10^{-8} \text{ cm}^3)$. The volume loss of all coatings is mainly caused by pure wear. In the coatings, the pure wear loss volume of S2 and S3 accounted for 96.70% and 94.13% of the total loss volume. This is due to the small change in dynamic current density compared to static current density, and the smaller effect of corrosion on S2 and S3. Therefore, the proportion of W in S2 and S3 to T is larger. The volume loss of 316 L is mainly affected by friction on corrosion, and the loss of (CrNbTiAlV) C_xN_y coatings volume is mainly affected by wear.

Stack et al. [56–58]. established a wear-corrosion mechanism diagram in the form of a function to explain the dominant role of friction and corrosion in tribo-corrosion experiments. In the process of tribo-corrosion, the factors affecting the material loss can be explained by Fig. 14(a). The dominant factor of material loss during tribo-corrosion can be analyzed by the ratio of the ΔW and the ΔC . Fig. 14(a) shows that the material loss of 316 L during tribo-corrosion is mainly affected by the corrosion increment. This is because during the experiment, the damage to the surface of 316 L by friction plating is relatively serious, and the current density of 316 L changes greatly,

resulting in a huge change in corrosion increment. The surface of the $(CrNbTiAlV)C_xN_y$ coating is protected by carbonitride, the surface state changes little and the current density changes little. So the T of the coatings is less affected by corrosion. The T of the coating is dominated by pure wear.

 W_C is the synergistic effect of corrosion on wear. Generally, the degree of synergistic effect in the tribo-corrosion process can be evaluated by the ratio of W_C to W. When the ratio is less than 1, it is defined as a low synergistic effect. When the ratio is greater than 10, it is defined as high synergistic effect. The ratio between 1 and 10 is medium synergistic effect. As shown in Fig. 14(b), all the samples are in the region of low synergistic effect, indicating that corrosion has little effect on wear, which is attributed to their good corrosion resistance. However, the corrosion current density of 316 L greatly decreases (two orders of magnitude, shown in Table 3) under the action of friction, which will further accelerate the progress of wear to a certain extent. On the contrary, due to the excellent chemical stability of nitrogen-carbide coatings, their corrosion current density decreases less under friction. Therefore, the synergistic effect of (CrNbTiAlV)C_xN_y coatings is weaker than that of 316 L substrate and falls higher in the diagram.

4. Conclusions

A series of (CrNbTiAlV) C_xN_y coatings were prepared on 316 L. The microstructure, crystal structure composition, and tribo-corrosion performance of the samples were studied. The following conclusions can be drawn from this study:

- The doping of carbon makes the coating structure dense and does not show columnar structure, and the sp³ clusters in the coating gradually increases.
- (2) The increase in carbon content enhances the hardness and elastic modulus of the coatings. The fracture resistance and plastic deformation resistance of the coating are gradually enhanced.
- (3) During the tribo-corrosion experiment, the electrochemical performance of all coatings is better than that of 316 L. The increase of carbon content in the coating reduces the friction coefficient of the coating to 0.28. In the static polarization test, S2 has the smallest current density $(1.68 \times 10^{-8} \text{ A/cm}^2)$. S4 exhibits the smallest current density in the PDP test $(1.68 \times 10^{-8} \text{ A/cm}^2)$. The dynamic current density of S4 changes the least $(0.14 \times 10^{-8} \text{ A/cm}^2)$ compared to the static current density due to the increase of the surface amorphous graphitic phase.
- (4) The carbonitride phase makes the corrosion resistance of the coating better than that of 316 L, and the sensitivity of friction to corrosion effects is lower than that of 316 L. Therefore, during the tribo-corrosion test, the volume loss of the coating is mainly pure wear. The coating is less affected by the synergistic effect of friction and corrosion than 316 L

Declaration of Competing Interest

The authors declare that they have no known competing financial interests or personal relationships that could have appeared to influence the work reported in this paper.

Data Availability

Data will be made available on request.

Acknowledgments

The authors gratefully acknowledge the financial support of National Natural Science Foundation of China (51835012, 51975554), the National Key Research and Development Plan of China (No. 2018YFB0703803), the Natural Science Foundation of Gansu Province (21JR7RA081), the basic research projects (2020-JCJQ-ZD-155-12) and CAS "Light of West China".

References

- Hansson CM. The impact of corrosion on society. Metall Mater Trans A 2011;42A: 2952–62.
- [2] Lindgren M, Siljander S, Suihkonen R, Pohjanne P, Vuorinen J. Erosion-corrosion resistance of various stainless steel grades in high-temperature sulfuric acid solution. Wear 2016;364:10–21.
- [3] Zeng L, Guo XP, Zhang GA, Chen HX. Semiconductivities of passive films formed on stainless steel bend under erosion-corrosion conditions. Corros Sci 2018;144: 258–65.
- [4] Cui Z, Wang L, Ni H, Hao W, Man C, Chen S, et al. Influence of temperature on the electrochemical and passivation behavior of 2507 super duplex stainless steel in simulated desulfurized flue gas condensates. Corros Sci 2017;118:31–48.
- [5] Sheu HH, Lee HB, Jian SY, Hsu CY, Lee CY. Investigation on the corrosion resistance of trivalent chromium conversion passivate on electroplated Zn-Ni alloy. Surf Coat Technol 2016;305:241–8.
- [6] Gill SK, Sure J, Wang Y, Layne B, He L, Mahurin S, et al. Investigating corrosion behavior of Ni and Ni-20Cr in molten ZnCl2. Corros Sci 2021;179:109105.
- [7] Dai NW, Zhang LC, Zhang JX, Zhang X, Ni QZ, Chen Y, et al. Distinction in corrosion resistance of selective laser melted Ti-6Al-4V alloy on different planes. Corros Sci 2016;111:703–10.
- [8] Dai NW, Zhang LC, Zhang JX, Chen QM, Wu ML. Corrosion behavior of selective laser melted Ti-6Al-4V alloy in NaCl solution. Corros Sci 2016;102:484–9.
- [9] Pang JJ, Liu FC, Liu J, Tan MJ, Blackwood DJ. Friction stir processing of aluminium alloy AA7075: microstructure, surface chemistry and corrosion resistance. Corros Sci 2016;106:217–28.
- [10] Ma Y, Zhou X, Liao Y, Yi Y, Wu H, Wang Z, et al. Localised corrosion in AA 2099-T83 aluminium-lithium alloy: the role of grain orientation. Corros Sci 2016;107: 41–8.
- [11] de B.-Lahovary M-L, Laffont L, Blanc C. Characterization of intergranular corrosion defects in a 2024 T351 aluminium alloy. Corros Sci 2017;119:60–7.

- [12] Niu DW, Zhang CX, Sui XD, Lu XL, Zhang X, Wang C, et al. Microstructure, mechanical properties and tribo-corrosion mechanism of (CrNbTiAlVMo)(x)N-1-(x) coated 316 L stainless steel in 3.5 wt% NaCl solution. Tribol Int 2022;173: 107638
- [13] Yeh JW, Chen SK, Lin SJ, Gan JY, Chin TS, Shun TT, et al. Nanostructured highentropy alloys with multiple principal elements: Novel alloy design concepts and outcomes. Adv Eng Mater 2004;6:299–303.
- [14] Yao Q, Thomas S, Gibson MA, Fraser HL, Birbilis N. Corrosion of high entropy alloys. npj Mater Degrad 2017;1:15.
- [15] Sohn SW, Liu YH, Liu JB, Gong P, Prades-Rodel S, Blatter A, et al. Noble metal high entropy alloys. Scr Mater 2017;126:29–32.
- [16] Gludovatz B, Ritchie RO. Fracture properties of high-entropy alloys. MRS Bull 2022;47:176–85.
- [17] Nair RB, Selvam K, Arora HS, Mukherjee S, Singh H, Grewal HS. Slurry erosion behavior of high entropy alloys. Wear 2017;386–387:230–8.
- [18] Lu ZP, Lei ZF, Huang HL, Liu SF, Zhang F, Duan DB, et al. Deformation Behavior and Toughening of High-Entropy Alloys. Acta Metall Sin 2018;54:1553–66.
- [19] Guo ZM, Zhang AJ, Han JS, Meng JH. Microstructure, mechanical and tribological properties of CoCrFeNiMn high entropy alloy matrix composites with addition of Cr3C2. Tribol Int 2020:151.
- [20] Zhang M, Zhang XH, Niu MY, Jiang ZS, Chen H, Sun YH. High-temperature tribological behavior of CoCrFeNiV high-entropy alloys: A parallel comparison with CoCrFeNiMn high-entropy alloys. Tribol Int 2022;174:107736.
- [21] Alvi S, Akhtar F. High temperature tribology of CuMoTaWV high entropy alloy. Wear 2019;426:412–9.
- [22] Shuang S, Ding ZY, Chung D, Shi SQ, Yang Y. Corrosion resistant nanostructured eutectic high entropy alloy. Corros Sci 2020;164:108315.
- [23] Zhang CX, Lu XL, Wang C, Sui XD, Wang YF, Zhou HB, et al. Tailoring the microstructure, mechanical and tribocorrosion performance of (CrNbTiAlV)N-x high-entropy nitride films by controlling nitrogen flow. J Mater Sci Technol 2022; 107:172–82.
- [24] Zhang CX, Lu XL, Zhou HB, Wang YF, Sui XD, Shi ZQ, et al. Construction of a compact nanocrystal structure for (CrNbTiAlV)N-x high-entropy nitride films to improve the tribo-corrosion performance. Surf Coat Technol 2022;429:127921.
- [25] Uporov S, Estemirova SK, Bykov VA, Zamyatin DA, Ryltsev RE. A single-phase ScTiZrHf high-entropy alloy with thermally stable hexagonal close-packed structure. Intermetallics 2020;122:106802.
- [26] Zhang H, He YZ, Pan Y, Guo S. Thermally stable laser cladded CoCrCuFeNi highentropy alloy coating with low stacking fault energy. J Alloy Compd 2014;600: 210–4.
- [27] Li W, Liu P, Liaw PK. Microstructures and properties of high-entropy alloy films and coatings: a review. Mater Res Lett 2018:6:199–229.
- [28] Si YX, Wang GG, Wen M, Tong Y, Wang WW, Li Y, et al. Corrosion and friction resistance of TiVCrZrWNx high entropy ceramics coatings prepared by magnetron sputtering. Ceram Int 2022;48:9342–52.
- [29] Xu WJ, Liao MD, Liu XH, Ji L, Ju PF, Li HX, et al. Microstructures and properties of (TiCrZrVAl)N high entropy ceramics films by multi-arc ion plating. Ceram Int 2021;47:24752–9.
- [30] Fang S, Wang C, Li CL, Luan JH, Jiao ZB, Liu CT, et al. Microstructures and mechanical properties of CoCrFeMnNiVx high entropy alloy films. J Alloy Compd 2020;820:153388.
- [31] Zheng SJ, Cai ZB, Pu JB, Zeng C, Chen SY, Chen R, et al. A feasible method for the fabrication of VAITiCrSi amorphous high entropy alloy film with outstanding anticorrosion property. Appl Surf Sci 2019;483:870–4.
- [32] Alamdari AA, Unal U, Motallebzadeh A. Investigation of microstructure, mechanical properties, and biocorrosion behavior of Ti1.5ZrTa0.5Nb0.5W0.5 refractory high-entropy alloy film doped with Ag nanoparticles. Surf Interfaces 2022;28:101617.
- [33] Khan NA, Akhavan B, Zhou HR, Chang L, Wang Y, Sun LX, et al. High entropy alloy thin films of AlCoCrCu0.5FeNi with controlled microstructure. Appl Surf Sci 2019; 495:143560
- [34] Astafurova EG, Reunova KA, Melnikov EV, Panchenko MY, Astafurov SV, Maier GG, et al. On the difference in carbon- and nitrogen-alloying of equiatomic FeMnCrNiCo high-entropy alloy. Mater Lett 2020;276:128183.
- [35] Xia A, Dedoncker R, Glushko O, Cordill MJ, Depla D, Franz R. Influence of the nitrogen content on the structure and properties of MoNbTaVW high entropy alloy thin films. J Alloy Compd 2021;850:156740.
- [36] El Garah M, Touaibia DE, Achache S, Michau AS, Sviridova EM, Postnikov PS, et al. Effect of nitrogen content on structural and mechanical properties of AlTiZrTaHf (-N) high entropy films deposited by reactive magnetron sputtering. Surf Coat Technol 2022;432:128051.
- [37] Khan NA, Akhavan B, Zhou CF, Zhou HR, Chang L, Wang Y, et al. High entropy nitride (HEN) thin films of AlCoCrCu0.5FeNi deposited by reactive magnetron sputtering. Surf Coat Technol 2020;402:126327.
- [38] Li H, Jiang N, Li JL, Huang JW, Kong J, Xiong DS. Hard and tough (NbTaMoW)N-x high entropy nitride films with sub-stoichiometric nitrogen. J Alloy Compd 2021; 889:161713.
- [39] Kao WH, Su YL, Horng JH, Wu HM. Effects of carbon doping on mechanical, tribological, structural, anti-corrosion and anti-glass-sticking properties of CrNbSiTaZr high entropy alloy coatings. Thin Solid Films 2021;717:138448.
- [40] Medina LZ, da Costa MVT, Paschalidou EM, Lindwall G, Riekehr L, Korvela M, et al. Enhancing corrosion resistance, hardness, and crack resistance in magnetron sputtered high entropy CoCrFeMnNi coatings by adding carbon. Mater Des 2021; 205:109711.

- [41] Lu XL, Zhang CX, Zhang X, Cao XJ, Kang J, Sui XD, et al. Dependence of mechanical and tribological performance on the microstructure of (CrAlTiNbV)Nx high-entropy nitride coatings in aviation lubricant. Ceram Int 2021;47:27342–50.
- [42] Niu YS, Wei J, Yu ZM. Microstructure and tribological behavior of multilayered CrN coating by arc ion plating. Surf Coat Technol 2015;275:332–40.
- [43] Zhang MD, Zhou F, Wang QZ, Fu YQ, Zhou ZF. Structural and tribological properties of CrMoCN coatings with various Mo contents in artificial seawater. Appl Surf Sci 2019;493:485–96.
- [44] Chen XC, Peng ZJ, Yu XA, Fu ZQ, Yue W, Wang CB. Microstructure and tribological performance of self-lubricating diamond/tetrahedral amorphous carbon composite film. Appl Surf Sci 2011;257:3180–6.
- [45] Ferrari AC, Robertson J. Raman spectroscopy of amorphous, nanostructured, diamond-like carbon, and nanodiamond. Philos Trans R Soc, A 2004;362: 2477–512.
- [46] Chu PK, Li LH. Characterization of amorphous and nanocrystalline carbon films. Mater Chem Phys 2006;96:253–77.
- [47] Wang YX, Wang LP, Xue QJ. Improving the tribological performances of graphite-like carbon films on Si3N4 and SiC by using Si interlayers. Appl Surf Sci 2011;257: 10246–53
- [48] Sun EHY. Tribocorrosion behaviour of low temperature plasma carburised 316L stainless steel in 0.5M NaCl solution. Corros Sci 2011;53:4131–40.
- [49] Celis PPJ-P, Wenger F. Tribo-corrosion of materials: Interplay between chemical, electrochemical, and mechanical reactivity of surfaces. Wear 2006;261:939–46.

- [50] Fu YQ, Zhou F, Wang QZ, Zhang MD, Zhou ZF. Electrochemical and tribocorrosion performances of CrMoSiCN coating on Ti-6Al-4V titanium alloy in artificial seawater. Corros Sci 2020;165:108385.
- [51] Andre Hatem JL, Wei Ronghua, Torres Ricardo D, Laurindo Carlos, Biscaia de Souza Gelson, Soares Paulo. Tribocorrosion behavior of low friction TiSiCN nanocomposite coatings deposited on titanium alloy for biomedical applications. Surf Coat Technol 2018;347:1–12.
- [52] Marian M, Tremmel S, Wartzack S, Song GC, Wang B, Yu JH, et al. Mxene nanosheets as an emerging solid lubricant for machine elements – Towards increased energy efficiency and service life. Appl Surf Sci 2020;523:146503.
- [53] Correa DRN, Kuroda PAB, Grandini CR, Rocha LA, Oliveira FGM, Alves AC, Toptan F. Tribocorrosion behavior of β-type Ti-15Zr-based alloys. Mater Lett 2016; 179:118–21.
- [54] Yan QZC, Xu YT, He WJ. Microstructure, phase and tribocorrosion behavior of 60NiTi alloy. Appl Surf Sci 2019;498:143838.
- [55] Watson SW, Friedersdorf FJ, Madsen BW, Cramer SD. Methods of measuring wearcorrosion synergism. Wear 1995;181–183:476–84.
- [56] Stack MM, Pungwiwat N. Erosion-corrosion mapping of Fe in aqueous slurries: some views on a new rationale for defining the erosion-corrosion interaction. Wear 2004;256:565–76.
- [57] Stack MM, Purandare Y, Hovsepian P. Impact angle effects on the erosion-corrosion of superlattice CrN/NbN PVD coatings. Surf Coat Technol 2004;188:556–65.
- [58] Stack MM, Abd El Badia TM. Mapping erosion-corrosion of WC/Co-Cr based composite coatings: particle velocity and applied potential effects. Surf Coat Technol 2006;201:1335–47.